J Mater Sci: Mater Electron (2018) 29:1304–1316
DOI 10.1007/s10854-017-8036-6

Growth process and enhanced photocatalytic performance of $CuBi_2O_4$ hierarchical microcuboids decorated with AuAg alloy nanoparticles

Fei Wang[1,2] · Hua Yang[1,2] · Haimin Zhang[2] · Jinlong Jiang[2]

Received: 19 August 2017 / Accepted: 11 October 2017 / Published online: 16 October 2017
© Springer Science+Business Media, LLC 2017

Abstract $CuBi_2O_4$ hierarchical microcuboids self-assembled from nanorods were synthesized via a coprecipitation method, and their growth process was investigated. The as-synthesized $CuBi_2O_4$ hierarchical microcuboids were decorated with AuAg alloy nanoparticles via a photocatalytic reduction method. The prepared samples were systematically investigated by XRD, SEM, TEM, XPS, UV–vis DRS, EIS, PL spectroscopy and photocurrent response. RhB was chosen as the target organic pollutant to evaluate the photocatalytic activity of the samples under simulated-sunlight irradiation. It is demonstrated that the prepared $CuBi_2O_4$ samples exhibit excellent photocatalytic activity toward the degradation of RhB. Furthermore, the decoration of AuAg alloy nanoparticles on $CuBi_2O_4$ hierarchical microcuboids leads to much enhanced photocatalytic performance of the resultant AuAg–$CuBi_2O_4$ composite. The main reason for this is that the recombination rate of photogenerated electron–hole pairs is decreased due to the electron transfer from $CuBi_2O_4$ microcuboids to AuAg nanoparticles, and thus more charges are able to participate in the photocatalytic reactions. The effect of ethanol (scavenger of ·OH), BQ (scavenger of $\cdot O_2^-$) and AO (scavenger of h^+) on the dye degradation and the yield of ·OH was also investigated. Based on the experimental results, it is confirmed that ·OH is the dominant reactive species responsible for the dye degradation. The underlying photocatalytic mechanism was discussed.

✉ Hua Yang
hyang@lut.cn

[1] State Key Laboratory of Advanced Processing and Recycling of Non-ferrous Metals, Lanzhou University of Technology, Lanzhou 730050, China

[2] School of Science, Lanzhou University of Technology, Lanzhou 730050, China

1 Introduction

Every year a huge amount of wastewater is generated from chemical industries like paper, textile, paint and cosmetic manufacturers all over the world. The industrial wastewater contains various organic dyes and pigments, most of which are non-biodegradable and carcinogenic and pose an immense threat to the environment and human health. Before the wastewater is discharged into the natural environment, the organic pollutants must be removed or destroyed into harmless inorganic substances. Various physical and chemical methods (e.g., adsorption, coagulation/flocculation, membrane filtration, electrolysis and advanced oxidation [1–5]) have been developed to decolorize the dye wastewater. Particularly, as one of advanced oxidation processes, semiconductor-based photocatalysis has received a great deal of interest because it allows the use of solar energy for the decomposition of dye pollutants and has been considered as a green technology for the wastewater treatment. The photocatalytic process is initiated by the irradiation of a semiconductor photocatalyst and the generation of charge carriers, i.e., holes (h^+) in the valence band (VB) and electrons (e^-) in the conduction band (CB). Those photogenerated electrons and holes that migrate to the semiconductor surface participate in the redox reactions and ultimately lead to the degradation of the organic pollutants. However, most of the photogenerated electrons and holes will undergo rapid geminate recombination, which limits the utilization rate of photons. Efficient separation of electron–hole pairs is crucial for achieving good photocatalytic activity of the semiconductor. Furthermore, in order to utilize solar energy more effectively in the photocatalysis, it is highly desirable to develop visible-light-responsive photocatalysts.

Bi-based oxide semiconductors are famously known to be an important class of visible-light-responsive photocatalysts

and have become a research hotspot in the field of photocatalysis. Structurally, the VB of Bi-based oxide semiconductors consists of O 2p and Bi 6s hybrid orbitals [6], which is different from the VB of other oxide semiconductors composed of merely O 2p states. Due to their unique band structure, Bi-based oxide semiconductors commonly exhibit high oxidative activity and charge-carrier mobility [7]. Examples of the most extensively studied Bi-based oxide semiconductors as visible light photocatalysts include $BiVO_4$, Bi_2WO_6 and Bi_2MoO_6 [6–10]. Recently, much work has been devoted to another Bi-based oxide semiconductor, copper bismuth oxide ($CuBi_2O_4$). $CuBi_2O_4$ is a p-type semiconductor and crystallizes in a spinel-type structure built up from square planar CuO_4 groups linked to distorted trigonal BiO_6 polyhedra [11]. Compared to the most famous TiO_2 photocatalyst with bandgap energy of 3.2 eV, $CuBi_2O_4$ has relatively smaller bandgap energy of 1.9 eV [12], implying that it can largely utilize the visible part of the solar spectrum. Furthermore, the CB potential of $CuBi_2O_4$ is more negative than the thermodynamic potential for water reduction. Due to these attractive features, $CuBi_2O_4$ has been extensively studied as a promising photocathode for solar water splitting into H_2 [13–17], as well as a promising visible light photocatalyst for the degradation of organic dye pollutants [18–23].

$CuBi_2O_4$ has been also frequently integrated with other semiconductors to form heterostructure composite photocatalysts with enhanced photocatalytic performance, such as $CuBi_2O_4/TiO_2$, $CuBi_2O_4/Bi_2WO_6$, $CuBi_2O_4$/SrO, $CuBi_2O_4/BiVO_4$, $CuBi_2O_4/NaTaO_3$ and $CuBi_2O_4/CeO_2$ [24–30]. In these composites, photogenerated electrons or holes tend to migrate from one semiconductor to another. This carrier transfer process leads to a decrease in the electron–hole recombination, and thus more electrons and/or holes are available for the photocatalytic reactions. It has been shown that these composite photocatalysts exhibited significantly enhanced photocatalytic activity compared to individual semiconductors. Another promising strategy to improve the photocatalytic activity of semiconductors is to decorate them with noble metals like Ag, Au and Pt [31–33]. The noble metals can act as efficient electron sinks to capture photogenerated electrons, thus leaving behind more photogenerated holes participating in the photocatalytic reactions. Moreover, the surface plasmon resonance (SPR) on metal nanoparticles could enhance the local electric field of neighboring semiconductors, which will facilitate the separation of photogenerated electrons and holes. Simultaneously, SPR-induced electrons and holes could also participate in the photocatalytic reactions. Up to now, however, there has been little work devoted to the photocatalytic performance of noble metal-decorated $CuBi_2O_4$ photocatalyst.

It is noted that the photocatalytic reaction dominantly occurs at the surface of the photocatalyst, implying that the morphology and microstructure of the photocatalyst has an important effect on its photocatalytic activity. Particularly, three dimensional (3D) self-assembled hierarchical architectures commonly exhibit superior light absorption efficiency due to enhanced light trapping by multiple scattering compared with solid particles. This indicates that 3D self-assembled hierarchical architectures are quite attractive for the application as the photocatalyst. To address the morphology-mediated tailoring of the performance of $CuBi_2O_4$, several 3D self-assembled hierarchical $CuBi_2O_4$ architectures have been fabricated, such as hierarchical nanoflowers [18], dumbbell-like architectures [34], hedgehog-like hierarchical architectures [35], and hierarchical microspheres comprised of nanorods or quadrilateral plates [22, 36]. We demonstrated that $CuBi_2O_4$ hierarchical microspheres synthesized via a coprecipitation method exhibited excellent electrochemical performance [36]. In this work, we synthesized another type of $CuBi_2O_4$ hierarchical architectures—microcuboids via a coprecipitation method. The synthesized $CuBi_2O_4$ hierarchical microcuboids were then decorated with AuAg alloy nanoparticles through a photocatalytic reduction method. It is noted that Ag nanoparticles have much stronger SPR than Au nanoparticles, but their chemical stability are inferior to Au nanoparticles [37]. Here we choose to use AuAg alloy nanoparticles as decorator with the aim of utilizing the advantage of both Ag and Au nanoparticles. The photocatalytic performance and mechanism of the as-prepared AuAg–$CuBi_2O_4$ composite was investigated by degrading rhodamine B (RhB) under simulated-sunlight irradiation.

2 Experimental

2.1 Synthesis of $CuBi_2O_4$ hierarchical microcuboids

All raw materials and chemical reagents used in the experiment were of analytical grade without further purification. In a typical synthesis procedure, 1.9402 g (0.004 mol) of $Bi(NO_3)_3{\cdot}5H_2O$, 0.4832 g (0.002 mol) of $Cu(NO_3)_2{\cdot}3H_2O$ and 2.982 g (0.04 mol) of KCl were successively dissolved in 20 mL of dilute nitric acid solution (2 mL HNO_3 + 18 mL distilled water), and the mixture was designated as solution A. 9.6 g (0.24 mol) of NaOH was dissolved in 60 mL of distilled water (solution B). The solution B was slowly added to the solution A drop by drop under constant stirring. The obtained mixture was then submitted to coprecipitation reaction for 0.5, 3, 6, 9 or 12 h under continuous stirring with a magnetic stirrer. The produced precipitate was collected by centrifugation, washed with distilled water and ethanol for four times, and dried at 60 °C for 12 h to obtain final $CuBi_2O_4$ product.

2.2 Preparation of AuAg-decorated $CuBi_2O_4$ microcuboids

The as-synthesized $CuBi_2O_4$ hierarchical microcuboids were decorated with AuAg alloy nanoparticles via a photocatalytic reduction route. 0.1 g of $CuBi_2O_4$ was loaded in 100 mL distilled water. 0.025 g of ammonium oxalate (AO) was dissolved in the $CuBi_2O_4$ suspension, followed by ultrasonic treatment for 5 min and then magnetic stirring for 50 min to make the particles disperse uniformly. To the suspension was slowly added 0.1 mL of $AgNO_3$ solution with concentration of 0.2 mol L^{-1} (M) and 0.38 mL of $HAuCl_4$ solution with concentration of 0.029 M. After magnetically stirred for 30 min, the mixture was exposed to ultraviolet (UV) light irradiation from a 15 W low-pressure mercury lamp for another 30 min under mild stirring. During the irradiation, Au^{3+} and Ag^+ ions were reduced to form AuAg alloy nanoparticles onto the surface of $CuBi_2O_4$ microcuboids. The product was collected and washed with distilled water for two times, followed by drying at 60 °C for 12 h to obtain final AuAg–$CuBi_2O_4$ composite.

2.3 Sample characterization

The crystal structure of the samples was determined by means of X-ray powder diffraction (XRD) with Cu Kα radiation ($\lambda = 0.15406$ nm). The morphology and microstructure of the samples was investigated by field-emission scanning electron microscopy (SEM) and field-emission transmission electron microscopy (TEM). The chemical state of elements in the samples was determined by X-ray photoelectron spectroscopy (XPS), where the binding energy scale of the XPS data was calibrated against the adventitious C 1s peak at the binding energy of 284.8 eV. The optical absorption and bandgap energy of the samples was investigated by ultraviolet–visible diffuse reflectance spectroscopy (UV–vis DRS) on a UV–vis spectrophotometer with an integrating sphere attachment by using $BaSO_4$ as the reference. The photoluminescence (PL) spectrum of the samples was measured on a fluorescence spectrophotometer with an excitation wavelength of 320 nm.

2.4 Photoelectrochemical measurement

The electrochemical impedance spectroscopy (EIS) and photocurrent response measurements were performed on a CST 350 electrochemical workstation using a three-electrode cell configuration, composed of a platinum foil as the counter electrode, a standard calomel electrode (SCE) as the reference electrode, and working electrode. To prepare the working electrode, 15 mg of $CuBi_2O_4$ or Ag–$CuBi_2O_4$, 0.75 mg of carbon black and 0.75 mg of polyvinylidene fluoride were mixed together using 1-methyl-2-pyrrolidione (NMP) as solvent to form slurry. The slurry was uniformly covered on fluorine-doped tin oxide glass substrate with area of 1×1 cm^2, which was then dried at 60 °C for 5 h in a thermostat drying oven. 0.1 M Na_2SO_4 aqueous solution was used as the electrolyte. A 200 W xenon lamp was used as the light source. The EIS measurement was carried out by applying the sinusoidal voltage pulse of amplitude of 5 mV and in the frequency range of 100 kHz to 0.01 Hz. The transient photocurrent measurement was performed at a bias voltage of 0.2 V.

2.5 Photocatalytic evaluation

The photocatalytic activity of the samples was evaluated by degrading RhB in aqueous solution under simulated-sunlight irradiation from a 200 W xenon lamp at room temperature. The initial concentration of RhB was 5 mg L^{-1}, and the catalyst loading was 0.1 g in 100 mL of RhB solution. Prior to irradiation, the reaction solution was magnetically stirred for 30 min in the dark in order to attain the adsorption/desorption equilibrium of RhB onto the photocatalyst surface. After that, 1 mL of H_2O_2 was added to the reaction solution, and was then irradiated by a 200 W xenon lamp. During the photocatalysis process, the reaction solution was maintained at room temperature by cooling the photocatalytic reactor with a water-cooling system. At intervals of 10 min, a small portion of the reaction solution was taken out for the examination of the RhB concentration. The RhB concentration was determined by measuring the absorbance of the reaction solution on a UV–vis spectrophotometer at a wavelength of 554 nm. Before measurement, the photocatalyst was removed by centrifugation at 4000 rpm for 10 min.

2.6 Examination of hydroxyl

Hydroxyl (·OH) radicals generated in the photocatalytic system were examined by PL spectroscopy using terephthalic acid (TPA) as a probe molecule. TPA will react with ·OH to produce 2-hydroxyterephthalic acid (TAOH), which has a unique fluorescence emission peak at 429 nm [38]. TPA was dissolved in 1.0 mM NaOH aqueous solution to make a 0.25 mM TPA solution. 0.1 g of the photocatalyst was loaded in 100 mL TPA solution, followed by magnetic stirring for 30 min in the dark. 1 mL of H_2O_2 was added to the reaction solution, which was then submitted to irradiation with a 200 W xenon lamp. After 30 min of reaction, a small portion of the solution was taken out for the PL measurement at a fluorescence spectrophotometer with an excitation wavelength of 315 nm. Before measurement, the reaction solution was centrifuged at 4000 rpm for 10 min to remove the photocatalyst.

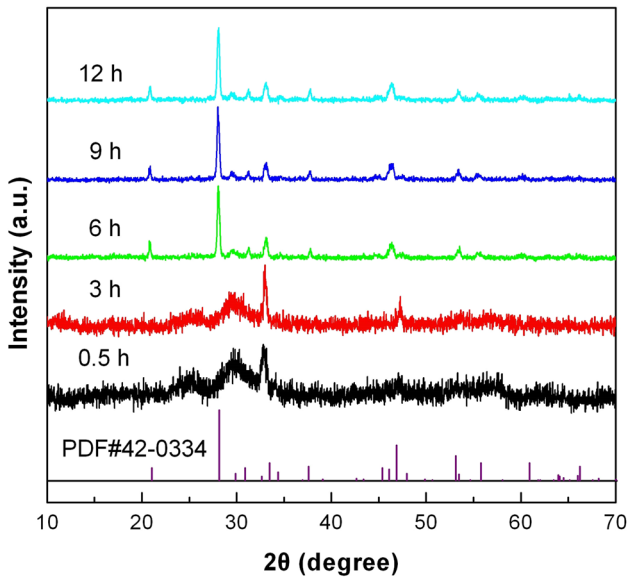

Fig. 1 XRD patterns of $CuBi_2O_4$ samples prepared at different reaction times, along with the standard XRD line pattern for $CuBi_2O_4$ tetragonal structure (PDF #42-0334)

3 Results and discussion

3.1 Growth process of $CuBi_2O_4$ hierarchical microcuboids

Figure 1 shows the XRD patterns of $CuBi_2O_4$ samples prepared at different reaction times (0.5, 3, 6, 9 and 12 h). It is seen that at the initial stage of the reaction, the obtained samples mainly present amorphous $Cu(OH)_2$ and $Bi(OH)_3$ precipitates. When the reaction time is increased up to 6 h, the amorphous precipitates are crystallized into $CuBi_2O_4$ nanocrystals. All the diffraction peaks for the sample can be indexed according to the standard diffraction pattern of PDF #42-0334, implying the formation of single $CuBi_2O_4$ tetragonal phase. With prolonging the reaction time, the diffraction peaks, particularly the widths of the diffraction peaks, of the obtained samples undergo almost no change, indicating that the size of $CuBi_2O_4$ grains remains the same.

Figure 2a–d show the SEM images of $CuBi_2O_4$ samples prepared at 3, 6, 9 and 12 h, respectively. At 3 h of reaction, the obtained product presents small-sized sphere-like, plate-like or rod-like particles, and these particles are

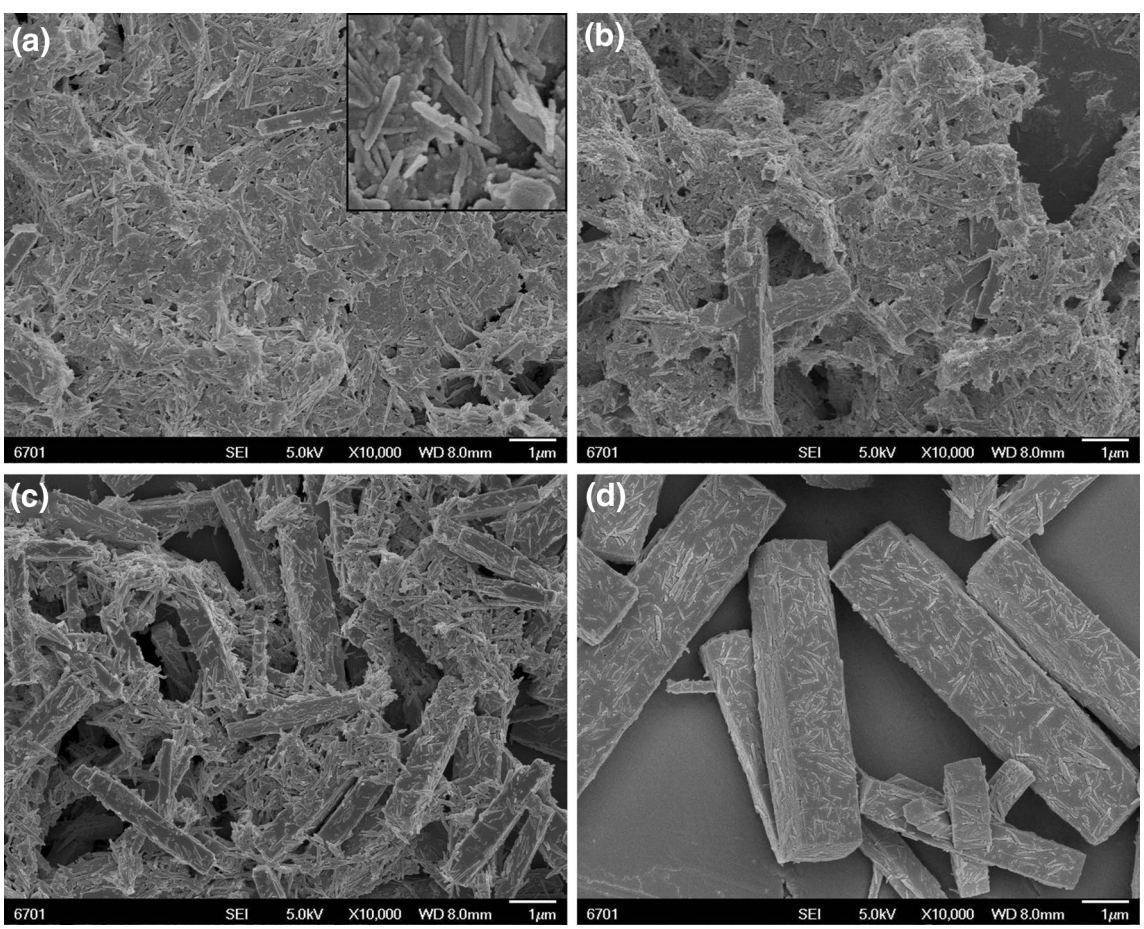

Fig. 2 SEM images of $CuBi_2O_4$ samples prepared at different reaction times. **a** 3 h; **b** 6 h; **c** 9 h; **d** 12 h

characterized by amorphous features. At 6 h of reaction, the amorphous particles are crystallized into $CuBi_2O_4$ nanorods, and furthermore, hierarchical microcuboids begin to form from the nanorods. With further increasing the reaction time, the formed $CuBi_2O_4$ nanorods gradually assemble into hierarchical microcuboids. When the reaction time is increased up to 12 h, it brings about the synthesis of regular $CuBi_2O_4$ hierarchical microcuboids with an average size of ~6 μm in length and ~1.5 μm in width.

Based on the XRD and SEM results, the formation process of $CuBi_2O_4$ hierarchical microcuboids is schematically illustrated in Fig. 3. It is noted that KCl plays an important role in the present synthesis of $CuBi_2O_4$ hierarchical microcuboids. When KCl is introduced to the reaction system, BiOCl precursor is formed at the initial stage of the reaction. The formation of BiOCl plays an important role in controlling the nucleation and growth process of $CuBi_2O_4$ nanocrystals. With the addition of NaOH solution to the reaction system, Bi^{3+} ions are slowly released from the BiOCl precursor to form amorphous $Bi(OH)_3$ precipitate, and simultaneously amorphous $Cu(OH)_2$ precipitate is also produced. These hydroxides are subject to the mineralizer (NaOH) attack to dissolve and form ion groups. In the region of supersaturated fluid, $CuBi_2O_4$ nuclei are formed and grow into nanorods. To reduce the overall surface energy, the freshly formed nanorods further self-assemble into hierarchical microcuboids.

Figure 4a shows the UV–vis DRS spectra of $CuBi_2O_4$ samples prepared at different reaction times, and Fig. 4b gives the corresponding first derivative spectra. The absorption edge of the samples related to the electron transition from VB to CB can be obtained from the peak in the first derivative spectra. It is seen that all the samples have a similar absorption edge at 660.1 nm, from which the bandgap energy E_g of the samples is obtained as 1.88 eV.

RhB was chosen as the organic pollutant to evaluate the photocatalytic activity of $CuBi_2O_4$ samples under simulated-sunlight irradiation, because RhB exhibits good stability under light exposure without photocatalyst. Figure 5a shows the time-dependent photocatalytic degradation of RhB over

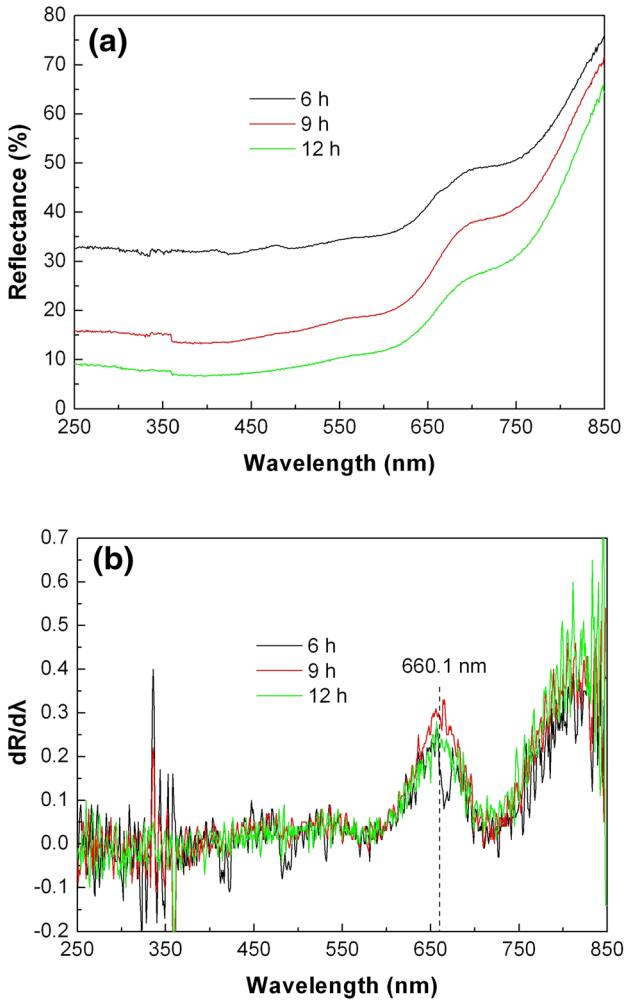

Fig. 4 **a** UV–vis DRS spectra of $CuBi_2O_4$ samples prepared at different reaction times. **b** The corresponding first derivative UV–vis DRS spectra

$CuBi_2O_4$ samples prepared at different reaction times. It is demonstrated that the samples exhibit a good photocatalytic activity toward the dye degradation. After 60 min of photocatalysis, 97% of the dye is observed to be degraded by the sample consisting of $CuBi_2O_4$ nanorods (prepared at 6 h).

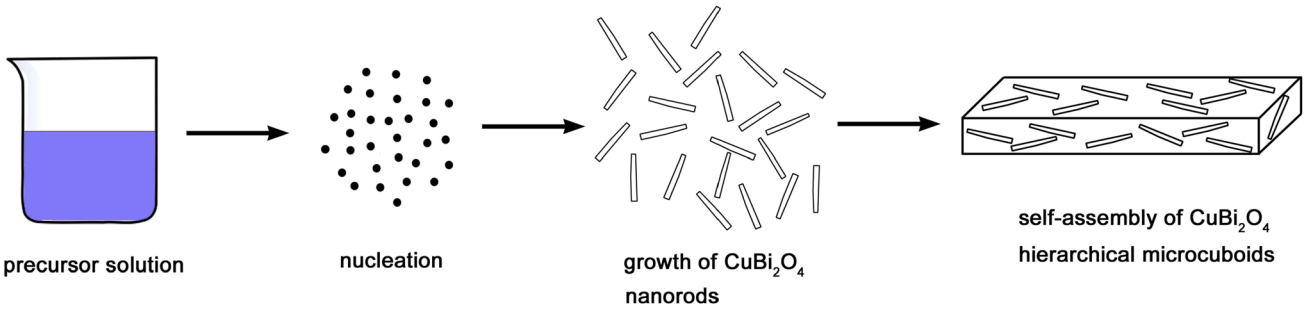

Fig. 3 Schematic illustration of the formation process of $CuBi_2O_4$ hierarchical microcuboids

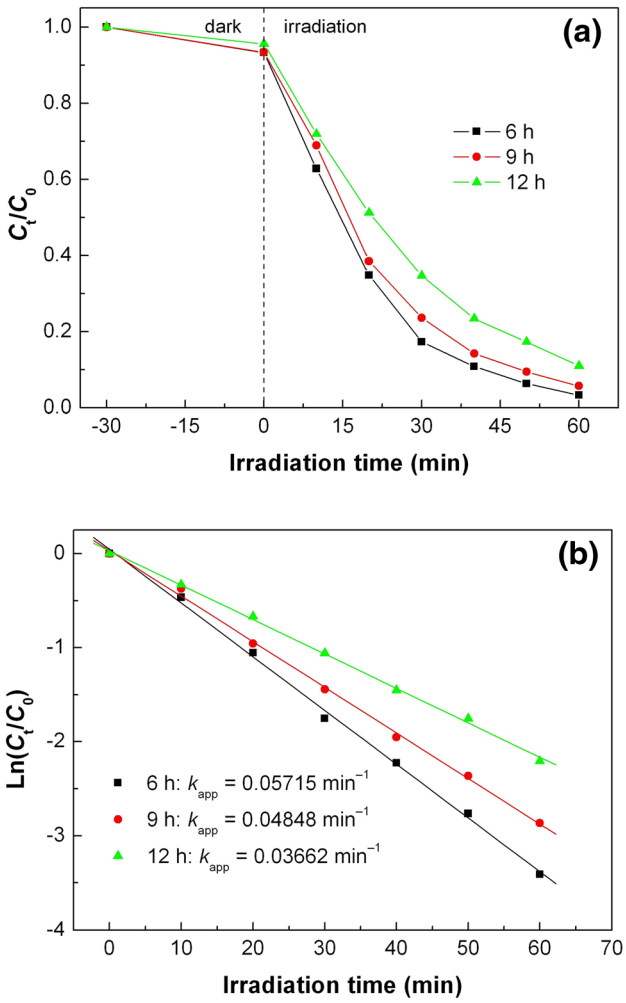

Fig. 5 **a** Time-dependent photocatalytic degradation of RhB over $CuBi_2O_4$ samples prepared at different reaction times under simulated-sunlight irradiation. **b** Plots of $Ln(C_t/C_0)$ versus irradiation time t for the $CuBi_2O_4$ samples

When $CuBi_2O_4$ nanorods self-assemble into hierarchical microcuboids, the resultant sample (prepared at 12 h) still possesses a high photocatalytic activity, where the degradation percentage of the dye reaches 89%. Figure 5b shows the plots of $Ln(C_t/C_0)$ versus irradiation time t. The dye degradation conforms well to the first-order kinetic equation $Ln(C_t/C_0) = -k_{app}t$, where k_{app} is the apparent first-order reaction rate constant (min^{-1}) [39]. The rate constants for the samples are obtained as 0.03662–0.05715 min^{-1}.

3.2 AuAg alloy nanoparticles-decorated $CuBi_2O_4$ hierarchical microcuboids

The photocatalytic performance of $CuBi_2O_4$ hierarchical microcuboids was further enhanced by the decoration of AuAg alloy nanoparticles through a photocatalytic reduction route. Figure 6a shows the XRD patterns of bare $CuBi_2O_4$ and AuAg–$CuBi_2O_4$ composite. It is seen that the decoration of AuAg alloy nanoparticles does not lead to the structural change in $CuBi_2O_4$, which maintains the tetragonal structure. Furthermore, additional weak diffraction peaks from AuAg alloy phase are visible in the XRD pattern of the composite, indicating the formation of AuAg alloy nanoparticles in the composite. Figure 6b shows the SEM image of AuAg–$CuBi_2O_4$, confirming that AuAg alloy nanoparticles with size of 20–30 nm are uniformly decorated onto the surface of $CuBi_2O_4$ microcuboids.

The microstructure of AuAg–$CuBi_2O_4$ composite was further investigated by TEM. Figure 7a shows the TEM image of AuAg–$CuBi_2O_4$, revealing good assembly of AuAg alloy nanoparticles on $CuBi_2O_4$ microcuboids. The TEM image also demonstrates that AuAg alloy nanoparticles are shaped like spheres and have a size distribution from 20 to 30 nm, which is in good agreement with the SEM

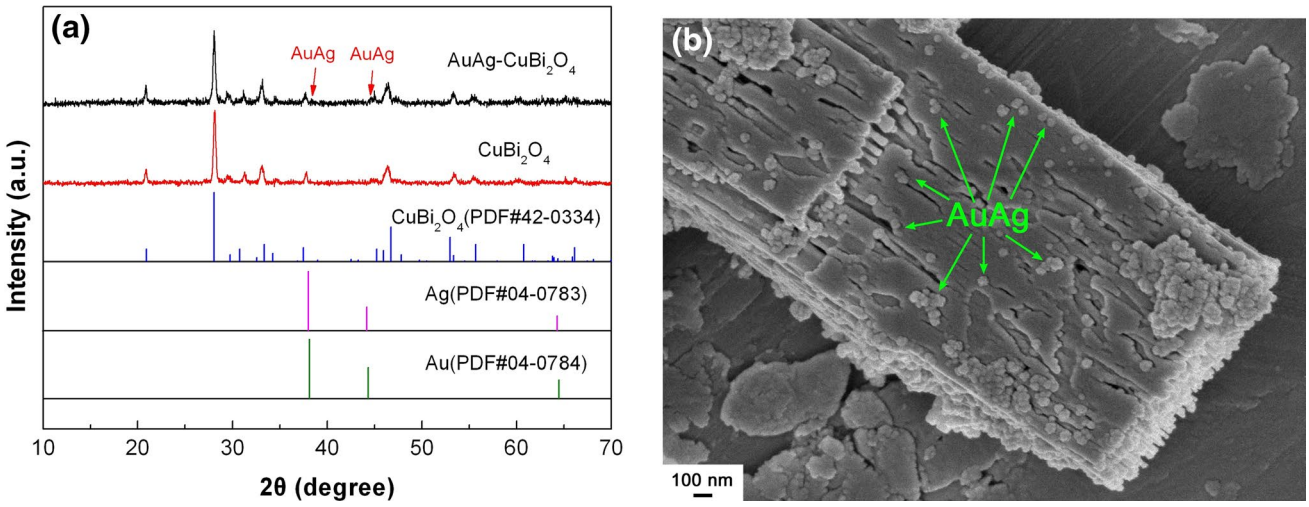

Fig. 6 **a** XRD patterns of bare $CuBi_2O_4$ and AuAg–$CuBi_2O_4$ composite. **b** SEM image of AuAg–$CuBi_2O_4$

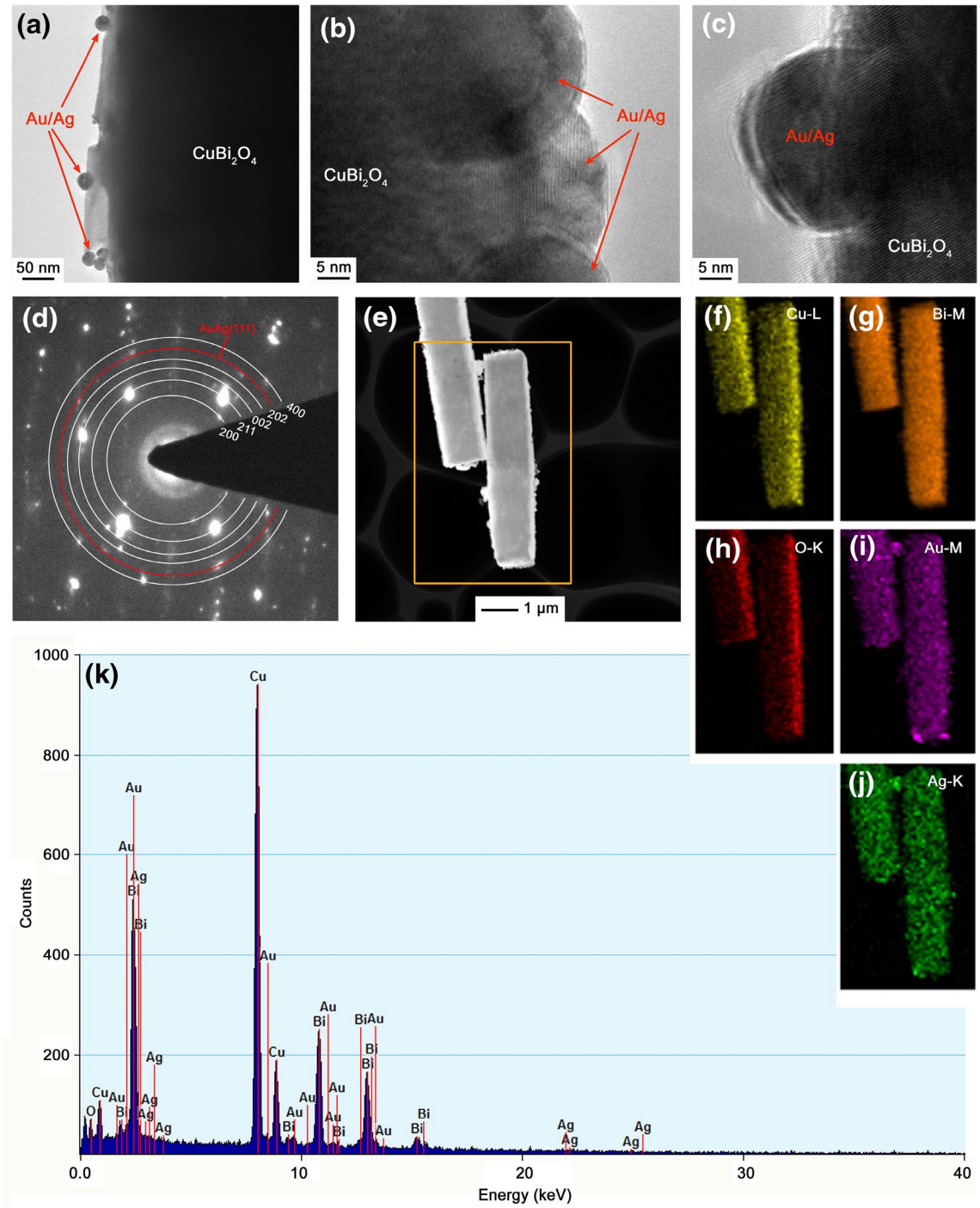

Fig. 7 **a** TEM image of AuAg–$CuBi_2O_4$. **b, c** HRTEM images of AuAg–$CuBi_2O_4$. **d** SAED pattern of AuAg–$CuBi_2O_4$. **e** DF-STEM image of AuAg–$CuBi_2O_4$. **f–j** The corresponding elemental mapping images of the region indicated in (**e**). **k** EDX spectrum of AuAg–$CuBi_2O_4$

observation result. Figure 7b, c show the high resolution TEM (HRTEM) images of AuAg–$CuBi_2O_4$. Perfect crystal lattice fringes are clearly visible for both $CuBi_2O_4$ microcuboids and AuAg nanoparticles, implying that they have a good crystallization with no or minor internal defects. Figure 7d shows the selected area electron diffraction (SAED) pattern of AuAg–$CuBi_2O_4$, which presents clearly concentric diffraction spots or diffraction rings. The diffraction spots can be indexed according to $CuBi_2O_4$ tetragonal phase and AuAg cubic phase. No diffraction spots assignable to other impurity phases are visible in the SAED pattern. This implies that $CuBi_2O_4$ microcuboids undergo no

structural change when decorated with AuAg alloy nanoparticles. Figure 7e shows the dark-field scanning TEM (DF-STEM) image of AuAg–$CuBi_2O_4$, and Fig. 7f–j give the corresponding elemental mapping images of the region indicated in Fig. 7d. The microcuboids clearly display the uniform elemental distribution of Cu, Bi and O. No obvious chemical composition segregation is observed in the $CuBi_2O_4$ phase. Furthermore, Au and Ag elements are seen to be uniformly distributed over the entire microcuboids, implying the assembly of uniform AuAg alloy nanoparticles onto $CuBi_2O_4$ microcuboids. The chemical composition of AuAg–$CuBi_2O_4$ is further investigated by the energy-dispersive X-ray spectroscopy (EDS). The obtained EDS spectrum is given in Fig. 7k, showing the presence of all the elements of the composite. The observation of extremely weak oxygen signal could be due to the fact that EDS is not sensitive to light elements [31]. The atomic ratio of Cu to Bi obtained from the EDS spectrum is much larger than the stoichiometric atomic ratio of Cu/Bi in the $CuBi_2O_4$ phase. The appearance of high-intensity Cu signal could be ascribed to an additional contribution of the Cu microgrid used for supporting the sample. The Au content is very similar to the Ag content, both of which account for about 2.1% of the total weight of AuAg–$CuBi_2O_4$ composite.

XPS was used to investigate the chemical state of the elements in $CuBi_2O_4$ and AuAg–$CuBi_2O_4$. Figure 8a shows the XPS survey scan spectra of the samples, both of which present the signals of the elements Cu, Bi and O. Moreover, additional Au and Ag signals appear on the XPS spectrum of the composite. Figure 8b–d show the high-resolution XPS spectra of Cu 2p, Bi 4f and O 1s, respectively. For bare $CuBi_2O_4$, the binding energies for Cu $2p_{3/2}$ and Cu $2p_{1/2}$ are observed at 934.7 and 954.7 eV, respectively, and furthermore, the Cu 2p peaks are accompanied by obvious satellite features (Fig. 8b). This confirms that the copper species exists in the Cu(II) oxidation state [14, 16]. On the Bi 4f XPS spectrum shown in Fig. 8c, the sharp peaks at 158.6 and 163.9 eV are assigned to the binding energies of Bi $4f_{7/2}$ and Bi 4 $f_{5/2}$, respectively, which implies that the bismuth species is in the form of Bi(III) oxidation state [14, 16]. The O 1s XPS signal shown in Fig. 8d is deconvoluted into three peaks separately at 529.7, 531.5 and 533.4 eV. The peak at 529.7 eV is assigned to the crystal lattice oxygen in $CuBi_2O_4$. The shoulder peaks at higher binding energies could arise due to surface defects or chemisorbed oxygen species [40]. For AuAg–$CuBi_2O_4$ composite, the Cu 2p binding energies exhibit a slight shift of 0.2 eV toward lower energy, whereas the Bi 4f and O 1s binding energies shift by 0.1–0.2 eV toward higher energy. This suggests a possible chemical bonding between $CuBi_2O_4$ and AuAg. Furthermore, the O 1s shoulder peaks also undergo a slight change in their intensity and position, indicating that the decoration of AuAg nanoparticles has an effect on the surface properties of $CuBi_2O_4$ hierarchical microcuboids. Figure 8e shows the Au 4f XPS spectrum, where the peaks at 84.1 and 87.8 eV are assigned to the binding energies for Au $4f_{7/2}$ and Au 4 $f_{5/2}$, respectively [41]. The Ag 3d XPS spectrum given in Fig. 8f shows two sharp peaks at 367.9 and 373.9 eV, which are attributed to the binding energies for Ag $3d_{5/2}$ and Ag $3d_{3/2}$, respectively [42]. The Au 4f and Ag 3d XPS spectra imply the existence of Au^0 and Ag^0 metal states. The oxidation states of Au and Ag species can be excluded because no additional peaks are visible on the XPS spectra.

Figure 9 shows the UV–vis DRS spectra of $CuBi_2O_4$ and AuAg–$CuBi_2O_4$. Compared to bare $CuBi_2O_4$, AuAg–$CuBi_2O_4$ composite has enhanced absorption in the visible light region, implying that the composite can utilize photons more effectively. The absorption edge of the samples can be derived from the peak on the first derivative spectra, as shown in the insert of Fig. 9. The composite has a similar absorption edge to that of bare $CuBi_2O_4$, implying a negligible change in the bandgap energy of $CuBi_2O_4$ hierarchical microcuboids when decorated with AuAg alloy nanoparticles.

PL spectroscopy was used to evaluate the recombination behavior of photogenerated electron–hole pairs in $CuBi_2O_4$ and AuAg–$CuBi_2O_4$. Figure 10 shows the PL spectra of the two samples measured at an excitation wavelength of 320 nm. For bare $CuBi_2O_4$, several PL emission peaks are clearly observed in the wavelength region of 400–550 nm. In contrast, the PL emission peaks from AuAg–$CuBi_2O_4$ become relatively weak, indicating a decrease in the electron–hole recombination. The efficient electron–hole separation can be ascribed to the electron transfer from $CuBi_2O_4$ microcuboids to AuAg nanoparticles. As a result, for AuAg–$CuBi_2O_4$ composite, more photogenerated electrons and holes are able to participate in the photocatalytic reactions.

The separation and transfer behavior of photogenerated electrons and holes for $CuBi_2O_4$ and AuAg–$CuBi_2O_4$ was further investigated via photocurrent response and EIS. Figure 11a shows the transient photocurrent response of the samples recorded for several on–off cycles under intermittent simulated sunlight irradiation. Upon turning on the simulated sunlight, an obvious photocurrent is observed for both the samples. When turning off the light, the photocurrent drops to an every low level (nearly to zero). Moreover, when the light is repeatedly switched between on and off, the transient photocurrent response appears to be highly reproducible. Compared to bare $CuBi_2O_4$, AuAg–$CuBi_2O_4$ composite displays an enhanced photocurrent density, indicating an increase in the electron–hole separation. Figure 11b shows the Nyquist plots of the EIS spectra for $CuBi_2O_4$ and AuAg–$CuBi_2O_4$, both of which exhibit a typical semicircle shape, and furthermore a relatively smaller semicircle diameter is observed for the composite. This implies that

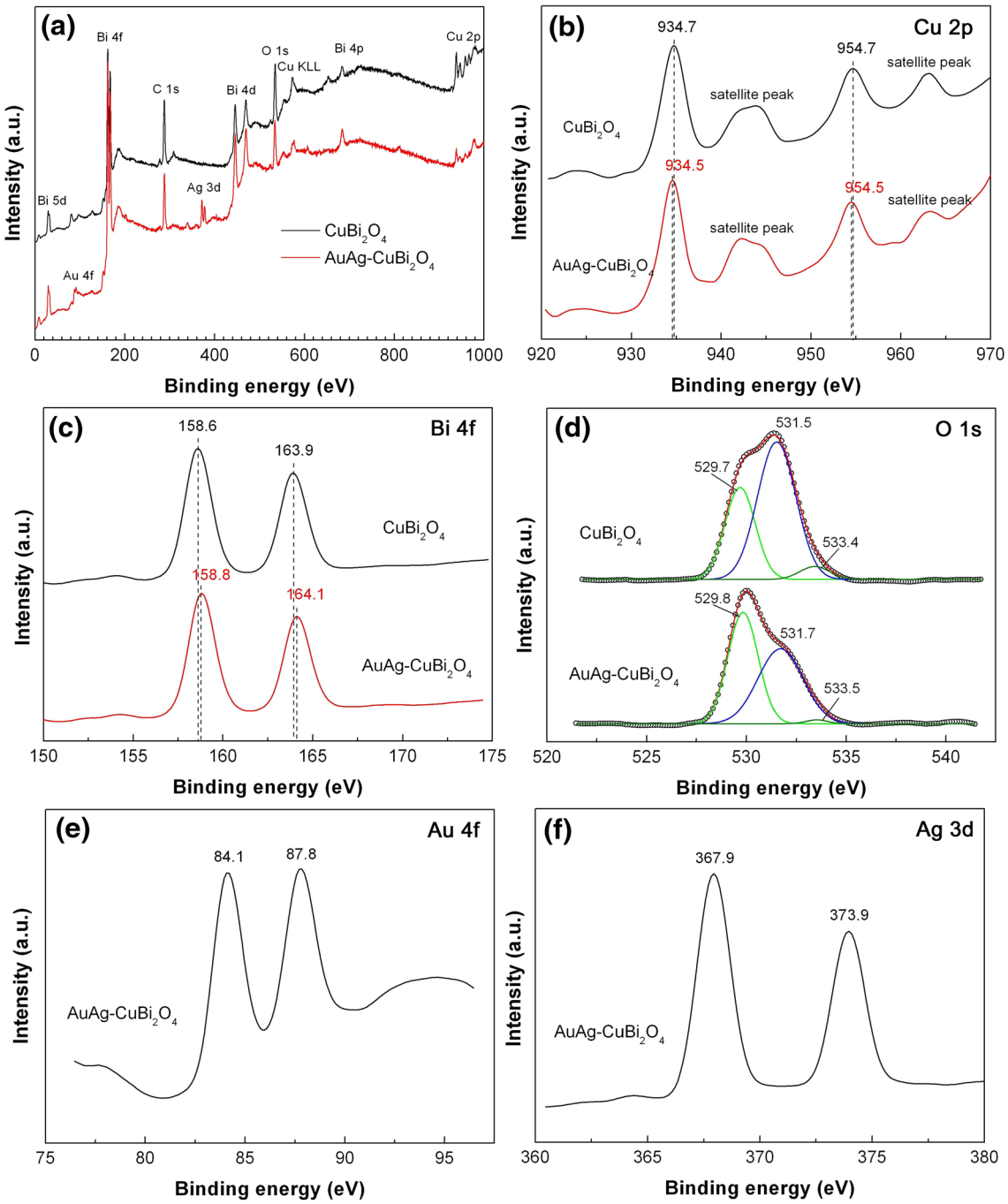

Fig. 8 XPS spectra of $CuBi_2O_4$ and AuAg–$CuBi_2O_4$. **a** XPS survey scan spectra; **b** Cu 2p XPS spectra; **c** Bi 4f XPS spectra; **d** O 1s XPS spectra; **e** Au 4f XPS spectrum; **f** Ag 3d XPS spectrum

the composite exhibits a smaller charge-transfer resistance. The smaller charge-transfer resistance suggests more efficient electron–hole separation and faster interface charge transfer occurring in the composite.

Figure 12a shows the time-dependent photocatalytic degradation of RhB over $CuBi_2O_4$ and AuAg–$CuBi_2O_4$ under simulated sunlight irradiation. The corresponding plots of $Ln(C_t/C_0)$ versus t and obtained rate constants k_{app} are inserted to Fig. 12a. It is obvious that AuAg–$CuBi_2O_4$ exhibits much higher photocatalytic activity than $CuBi_2O_4$. After 60 min of photocatalysis, the degradation percentage of the dye reaches 99% for AuAg–$CuBi_2O_4$, compared to 89% for $CuBi_2O_4$. From the reaction rate constants, it is concluded that AuAg–$CuBi_2O_4$ has a photocatalytic activity 1.9 times higher than that of $CuBi_2O_4$.

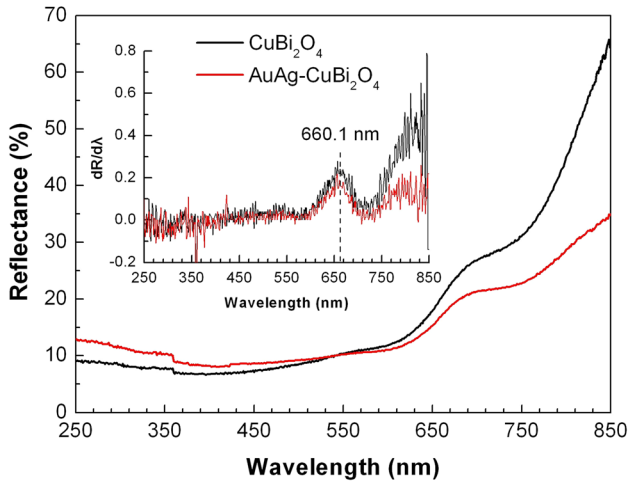

Fig. 9 UV–vis DRS spectra of $CuBi_2O_4$ and AuAg–$CuBi_2O_4$. The corresponding first derivative UV–vis DRS spectra are inserted to the figure

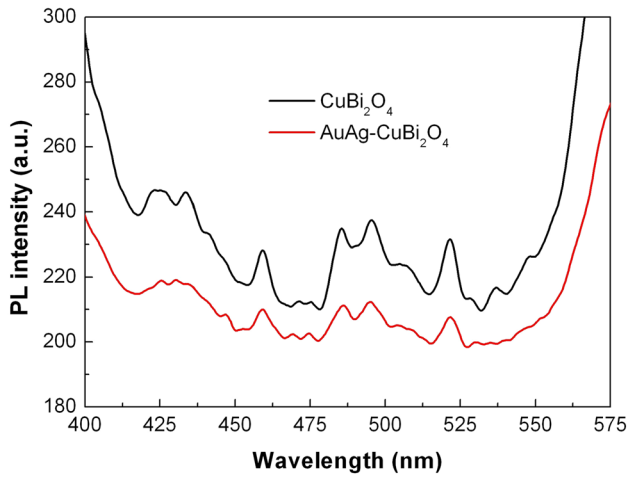

Fig. 10 PL spectra of $CuBi_2O_4$ and AuAg–$CuBi_2O_4$ measured at an excitation wavelength of 320 nm

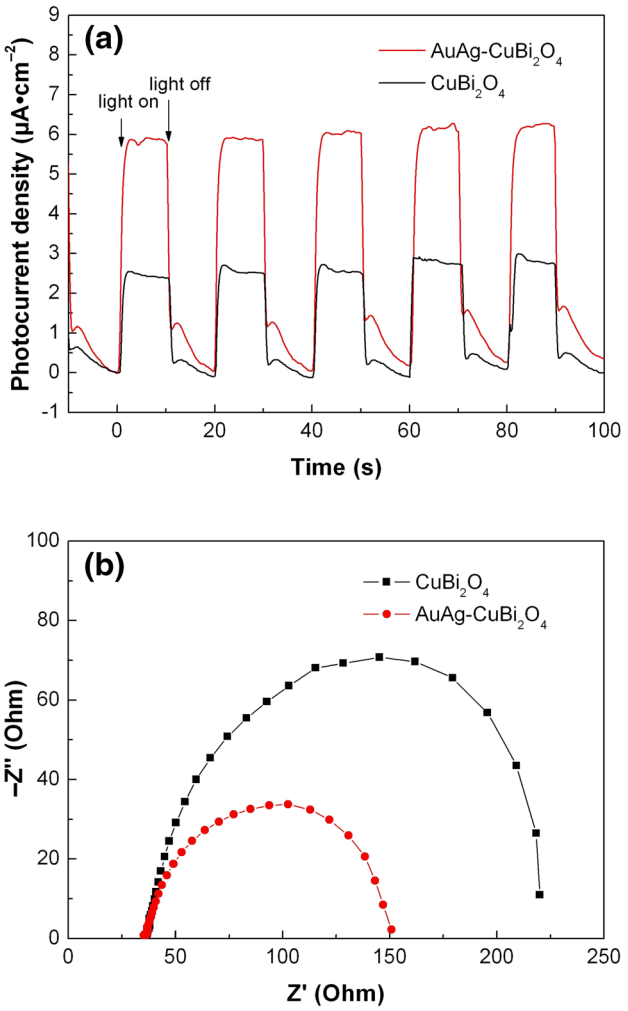

Fig. 11 **a** Transient photocurrent response of $CuBi_2O_4$ and AuAg–$CuBi_2O_4$ recorded for several on–off cycles under intermittent simulated sunlight irradiation. **b** Nyquist plots of the EIS spectra for $CuBi_2O_4$ and AuAg–$CuBi_2O_4$

The photocatalytic stability of AuAg–$CuBi_2O_4$ was investigated by the recycling photocatalytic experiment. After the first cycle of the photocatalysis was completed, AuAg–$CuBi_2O_4$ was collected and loaded in a fresh RhB solution for the next cycle of the photocatalytic experiment under the same conditions. Figure 12b shows the photocatalytic degradation of RhB over AuAg–$CuBi_2O_4$ repeatedly used for four times. At the 4th cycle of the photocatalysis, the degradation percentage of RhB remains a high value of 94% after 60 min of photocatalysis. This implies an excellent recycling stability of AuAg–$CuBi_2O_4$ composite.

To elucidate the role of ·OH, superoxide ($\cdot O_2^-$) and h^+ in the photocatalysis, we investigated the effect of ethanol, benzoquinone (BQ) and ammonium oxalate (AO) on the photocatalytic degradation of RhB, because ethanol, BQ and AO can be used as the scavengers of ·OH, $\cdot O_2^-$ and h^+, respectively [43]. 5 mL of ethanol, 0.1 mmol of BQ and 0.1 mmol of AO are separately added in 100 mL reaction solution, and then the photocatalytic experiments are carried out under the same conditions. Figure 12c shows the effect of the scavengers on the degradation of RhB over AuAg–$CuBi_2O_4$. It is found that the addition of ethanol or BQ to the reaction solution has a significant suppression on the dye degradation, where the slight decolorization is mainly attributed to the adsorption effect. This implies that the dye degradation is highly correlated with ·OH and $\cdot O_2^-$. On the addition of AO to the reaction solution, the dye degradation is observed to be slightly inhibited and still maintains a high level of 91% after 60 min of photocatalysis, indicating that h^+ plays only a minor role in the photocatalysis.

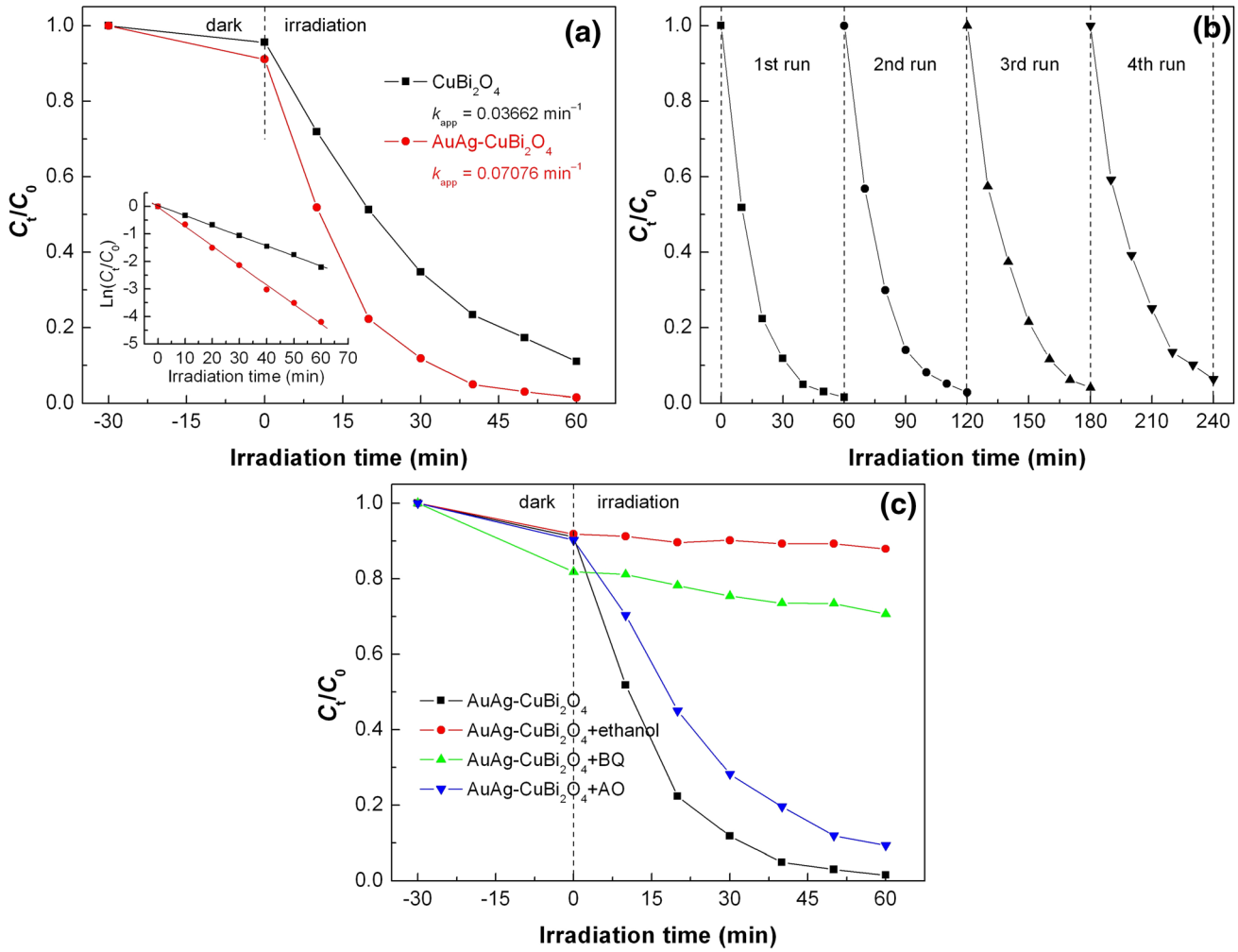

Fig. 12 **a** Time-dependent photocatalytic degradation of RhB over $CuBi_2O_4$ and AuAg–$CuBi_2O_4$ under simulated sunlight irradiation. **b** Photocatalytic degradation of RhB over AuAg–$CuBi_2O_4$ repeatedly used for four times. **c** Effect of ethanol, BQ and AO on the degradation of RhB over AuAg–$CuBi_2O_4$

To further confirm the reactive species, ·OH radicals produced in the simulated sunlight-irradiated AuAg–$CuBi_2O_4$ system were examined by PL spectroscopy using TPA as a probe for ·OH. Figure 13 shows the PL spectra of the TPA solution after reaction for 30 min over AuAg–$CuBi_2O_4$ with separately adding ethanol, BQ and AO. On irradiating AuAg–$CuBi_2O_4$ without adding the scavengers (ethanol, BQ and AO), the TPA solution shows a strong PL signal at around 429 nm, suggesting the production of ·OH in the present photocatalytic system. When adding AO to the TPA reaction solution, the intensity of the PL signal undergoes a minor decrease, implying that AO has only a slight suppression of the ·OH yield. On the addition of ethanol or BQ, the obtained PL spectrum is very similar to that of the blank TPA solution, where no obvious PL signal is observed. This implies that ·OH is quenched by ethanol or BQ. It is noted that the effect of ethanol, BQ and AO on the ·OH yield is

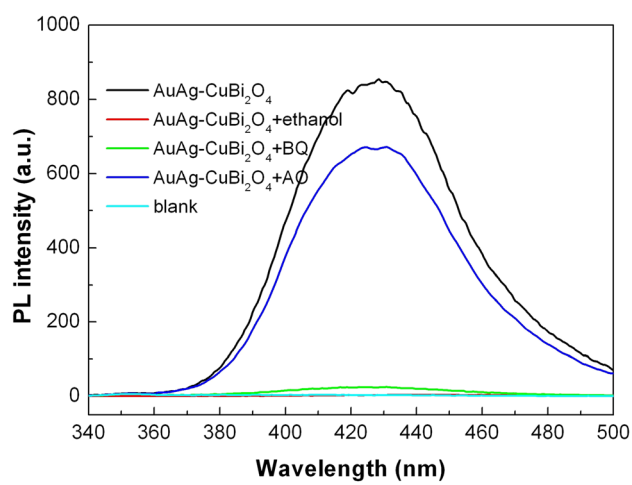

Fig. 13 Effect of ethanol, BQ and AO on the PL spectra of the TPA solution after reaction for 30 min over AuAg–$CuBi_2O_4$

very similar to their effect on the dye degradation. Based on this information, it is deduced that ·OH is the dominant reactive species causing the dye degradation.

In order to understand the photocatalytic mechanism of AuAg–$CuBi_2O_4$ composite, it is useful to determine the potential energy diagram of the composite. The flat band potential of $CuBi_2O_4$ can be derived using the Mott–Schottky equation [44].

$$\frac{1}{C^2} = \left(\frac{2}{e\varepsilon_r\varepsilon_0 N_d A}\right)\left(V - V_{FB} - \frac{kT}{e}\right) \quad (1)$$

where C is the space charge capacitance, e electron charge, ε_r relative permittivity, ε_0 vacuum permittivity, N_d majority carrier density, A electrode surface area, V applied potential, V_{FB} flat band potential, k Boltzmann constant, and T absolute temperature. The space charge capacitance of $CuBi_2O_4$ is obtained by electrochemical impedance measurements in the dark [45]. Figure 14a shows the Mott–Schottky plots of $CuBi_2O_4$ measured at 3000 and 5000 Hz. The flat band potential (V_{FB}) can be derived by extrapolating the linear portion of the plots to the potential axis (here kT/e is negligible due to its small value). At both frequencies, a similar V_{FB} value is obtained as 0.87 V versus SCE. Furthermore, the negative slope implies that $CuBi_2O_4$ is a p-type semiconductor. The potential is measured against an SCE reference at pH 7 and converted to the potential at normal hydrogen electrode (NHE) according to the relationship $V(\text{NHE}) = V(\text{SCE}) + 0.059\text{pH} + 0.242$. Assuming that the gap between the flat band potential and the top edge of the VB is negligible, the VB and CB potentials of $CuBi_2O_4$ are estimated as indicated in Fig. 14b. It is generally accepted that the Fermi level of AuAg alloy nanoparticles is located at +(0.4–0.45) V versus NHE [46, 47], which is more positive than the CB potential of $CuBi_2O_4$ hierarchical microcuboids. This implies that the photogenerated electrons thermodynamically favor the migration from $CuBi_2O_4$ microcuboids to AuAg nanoparticles. This electron transfer process leads to an efficient electron–hole separation, and thus more charge carriers are able to participate in the photocatalytic reactions. As a result, AuAg–$CuBi_2O_4$ composite exhibits an enhanced photocatalytic performance compared to bare $CuBi_2O_4$. It is confirmed from the above experimental results and analyses that ·OH is the dominant reactive species in the AuAg–$CuBi_2O_4$ photocatalytic system. There are several possible paths to produce ·OH in a photocatalytic system. The most common route is through combination of the photogenerated h^+ with OH^- or H_2O to produce ·OH, but this route can be largely excluded in the present photocatalytic system since the quenching of h^+ by the scavenger AO leads to only a slight suppression of the ·OH yield. Furthermore, the VB potential of $CuBi_2O_4$ is more negative than the redox potentials of OH^-/·OH (+1.89 vs. NHE) and H_2O/·OH (+2.72 V vs. NHE) [48]. This suggests that, from a thermodynamic point of view, the photogenerated h^+ cannot react with OH^- or H_2O to produce ·OH. On the other hand, when $\cdot O_2^-$ is quenched by BQ, almost no ·OH is observed to be formed. This implies that the generation of ·OH is highly dependent on $\cdot O_2^-$. The main reactions involved in the photocatalytic process can be briefly described as follows.

$$CuBi_2O_4 + h\nu \rightarrow CuBi_2O_4(e^- + h^+) \quad (2)$$

$$O_2 + e^- \rightarrow \cdot O_2^- \quad (3)$$

$$H_2O_2 + \cdot O_2^- \rightarrow \cdot OH + OH^- + O_2 \quad (4)$$

$$\cdot OH + RhB \rightarrow \text{degradation product} \quad (5)$$

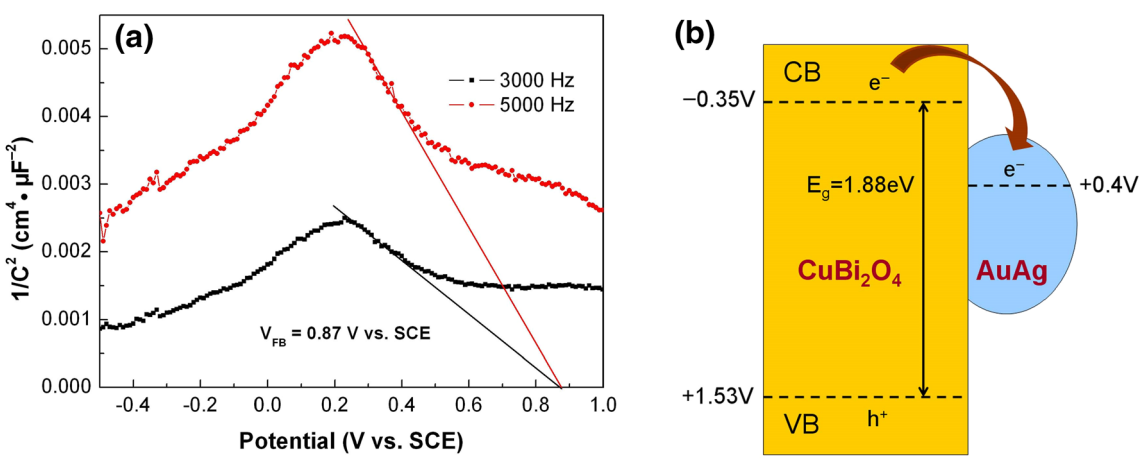

Fig. 14 **a** Mott–Schottky plots of $CuBi_2O_4$ obtained at 3000 and 5000 Hz. **b** Schematic illustration of the potential energy diagram for AuAg–$CuBi_2O_4$ composite

4 Conclusions

Regular $CuBi_2O_4$ hierarchical microcuboids with an average size of ~6 μm in length and ~1.5 μm in width were synthesized by a coprecipitation method. The hierarchical microcuboids are formed by self-assembly from nanorods. AuAg alloy nanoparticles with size of 20–30 nm were decorated on the surface of $CuBi_2O_4$ hierarchical microcuboids through a photocatalytic reduction method. The formed AuAg–$CuBi_2O_4$ composite exhibits an excellent photocatalytic activity toward the degradation of RhB under simulated-sunlight irradiation, which is about 1.9 times higher than that of bare $CuBi_2O_4$ hierarchical microcuboids. It is observed that AuAg–$CuBi_2O_4$ composite has an enhanced separation efficiency of photogenerated electron–hole pairs due to the electron migration from $CuBi_2O_4$ microcuboids to AuAg alloy nanoparticles. As a result, more photogenerated charges can be used for participation in the photocatalytic reactions. From the effect of ethanol, BQ and AO on the dye degradation and the yield of ·OH, it is concluded that ·OH is the dominant reactive species responsible for the dye degradation, and the production of ·OH is highly dependent on $\cdot O_2^-$.

Acknowledgements This work was supported by the National Natural Science Foundation of China (Grant No. 51662027).

References

1. E. Bazrafshan, M.R. Alipour, A.H. Mahvi, Desalin. Water Treat. **57**, 9203 (2016)
2. C.Z. Liang, S.P. Sun, F.Y. Li, Y.K. Ong, T.S. Chung, J. Membr. Sci. **469**, 306 (2014)
3. H.C. Wang, H.Y. Cheng, S.S. Wang, D. Cui, J.L. Han, Y.P. Hu, S.G. Su, A.J. Wang, J. Environ. Sci. **39**, 198 (2016)
4. P.A. Soares, T.F.C.V. Silva, D.R. Manenti, S.M.A.G.U. Souza, R.A.R. Boaventura, V.J.P. Vilar, Environ. Sci. Pollut. R **21**, 932 (2014)
5. S. Ahmed, M.G. Rasul, W.N. Martens, R. Brown, M.A. Hashib, Desalination **261**, 3 (2010)
6. M. Oshikiri, M. Boero, J.H. Ye, Z.G. Zou, G.Y. Kido, J. Chem. Phys. **117**, 7313 (2002)
7. A. Kudo, K. Omori, H. Kato, J. Am. Chem. Soc. **121**, 11459 (1999)
8. Y.H. Zhang, N. Zhang, Z.R. Tang, Y.J. Xu, Chem. Sci. **4**, 1820 (2013)
9. T. Saison, P. Gras, N. Chemin, C. Chaneac, O. Durupthy, V. Brezova, C. Colbeau-Justin, J.P. Jolivet, J. Phys. Chem. C **117**, 22656 (2013)
10. Y.C. Hao, X.L. Dong, S.R. Zhai, X.Y. Wang, H.C. Ma, X.F. Zhang, Chem. Commun. **52**, 6525 (2016)
11. N. Henry, O. Mentre, J.C. Boivin, F. Abraham, Chem. Mater. **13**, 543 (2001)
12. F. Wang, H. Yang, Y.C. Zhang, R.S. Li, Int. J. Mater. Res. **108**, 298 (2017)
13. R. Patil, S. Kelkar, R. Naphade, S. Ogale, J. Mater. Chem. A **2**, 3661 (2014)
14. Y. Nakabayashi, M. Nishikawa, Y. Nosaka, Electrochim. Acta **125**, 191 (2014)
15. D.W. Cao, N. Nasori, Z.J. Wang, Y. Mi, L.Y. Wen, Y. Yang, S.C. Qu, Z.G. Wang, Y. Lei, J. Mater. Chem. A **4**, 8995 (2016)
16. S.P. Berglund, F.F. Abdi, P. Bogdanoff, A. Chernseddine, D. Friedrich, R. van de Krol, Chem. Mater. **28**, 4231 (2016)
17. Y.H. Choi, K.D. Yang, D.H. Kim, K.T. Nam, S.H. Hong, Mater. Lett. **188**, 192 (2017)
18. Y. Zhang, Y. Xie, J. Li, G. Yang, T. Bai, J. Wang, J. Alloys Compd. **580**, 172 (2013)
19. Y. Xie, Y. Zhang, G. Yang, C. Liu, J. Wang, Mater. Lett. **107**, 291 (2013)
20. S. Anandan, N. Pugazhenthiran, G.J. Lee, J.J. Wu, J. Mol. Catal. A **379**, 112 (2013)
21. Y.F. Zhang, G.F. Li, H.P. Zhao, F. Tian, S.Q. Xiao, R. Chen, CrystEngComm **15**, 8159 (2013)
22. X.J. Chen, Y.Z. Dai, J. Guo, Mater. Lett. **161**, 251 (2014)
23. J.W. Zhang, Y.Y. Jiang, J. Mater. Sci. **26**, 4308 (2015)
24. W. Liu, S. Chen, S. Zhang, W. Zhao, H. Zhang, X. Yu, J. Nanopart. Res. **12**, 1355 (2010)
25. Y. Zhang, Y. Xie, J. Li, T. Bai, J. Wang, J. Sol-Gel Sci. Technol. **71**, 38 (2014)
26. W. Liu, S. Chen, H. Zhang, X. Yu, J. Exp. Nanosci. **6**, 102 (2011)
27. E. Abdelkader, L. Nadjia, B. Ahmed, Appl. Surf. Sci. **258**, 5010 (2012)
28. M. Nishikawa, S. Hiura, Y. Mitani, Y. Nosaka, J. Photochem. Photobiol. A **262**, 52 (2013)
29. Y. Deng, Y. Chen, B. Chen, J. Ma, J. Alloys Compd. **559**, 116 (2013)
30. A. Elaziouti, N. Laouedj, A. Bekka, R.N. Vannier, Sci. Technol. **39**, 9 (2014)
31. Y.C. Ye, H. Yang, R.S. Li, X.X. Wang, J. Sol-Gel Sci. Technol. **82**, 509 (2017)
32. J. Park, S. Park, R. Selvaraj, Y. Kim, RSC Adv. **5**, 52737 (2015)
33. L.B. Di, Z.J. Xu, K. Wang, X.L. Zhang, Catal. Today **211**, 109 (2013)
34. M. Wang, J. Zai, X. Wei, W. Chen, N. Liang, M. Xu, R. Qi, X. Qian, CrystEngComm **17**, 4019 (2015)
35. W.D. Oha, S.K. Lua, Z. Dong, T.T. Lim, Nanoscale **8**, 2046 (2016)
36. Y.C. Zhang, H. Yang, W.P. Wang, H.M. Zhang, R.S. Li, X.X. Wang, R.C. Yu, J. Alloys Compd. **684**, 707 (2016)
37. C. Gao, Y. Hu, M. Wang, M. Chi, Y. Yin, J. Am. Chem. Soc. **136**, 7474 (2014)
38. M. Zhou, H. Yang, T. Xian, R.S. Li, H.M. Zhang, X.X. Wang, J. Hazard. Mater. **289**, 149 (2015)
39. I.K. Konstantinou, T.A. Albanis, Appl. Catal. B **49**, 1 (2004)
40. W.P. Wang, H. Yang, T. Xian, J.L. Jiang, Mater. Trans. **53**, 1586 (2012)
41. J. Li, S. Meng, T. Wang, Q. Xu, L. Shao, D. Jiang, M. Chen, Appl. Surf. Sci. **396**, 430 (2017)
42. W. Teng, X. Li, Q. Zhao, G. Chen, J. Mater. Chem. A **1**, 9060 (2013)
43. T. Xian, H. Yang, L.J. Di, J.F. Dai, J. Alloys Compd. **622**, 1098 (2015)
44. F. Cardon, W.P. Gomes, J. Phys. D **11**, L63 (1978)
45. M.C. Fabrice, W.P. Royston, M. Benoit, M. Mario, Chem. Mater. **21**, 3752 (2009)
46. P.V. Kamat, J. Phys. Chem. C **111**, 2834 (2007)
47. V. Subramanian, E.E. Wolf, P.V. Kamat, J. Am. Chem. Soc. **126**, 4943 (2004)
48. T. Tachikawa, M. Fujitsuka, T. Majima, J. Phys. Chem. C **111**, 5259 (2007)